

Mapping the multiphase structure of H I in the Low-Latitude Intermediate-Velocity Arch 1

2 LUKA VUJEVA ,^{1,2,3,4} ANTOINE MARCHAL ,^{2,5} PETER G. MARTIN ,² AND MUKESH TAANK ,^{2,6}

3 ¹*Department of Astronomy and Astrophysics, University of Toronto, 60 St. George Street, Toronto, ON M5S 3H8, Canada*

4 ²*Canadian Institute for Theoretical Astrophysics, University of Toronto, 60 St. George Street, Toronto, ON M5S 3H8, Canada*

5 ³*Cosmic DAWN Centre (DAWN), Niels Bohr Institute, University of Copenhagen, Jagtvej 128, DK-2200 Copenhagen N*

6 ⁴*Niels Bohr Institute, University of Copenhagen, Lyngbyvej 2, DK-2100 Copenhagen Ø*

7 ⁵*Research School of Astronomy & Astrophysics, Australian National University, Canberra ACT 2610 Australia*

8 ⁶*Department of Mathematics and Statistics, University of Guelph, 50 Stone Road E., Guelph, ON N1G 2W1, Canada*

9 (Received March 5, 2023; Revised --, --; Accepted --, --)

10 Submitted to ApJ

ABSTRACT

12 We have analyzed the thermal and turbulent properties of the Low-Latitude Intermediate-Velocity Arch 1
13 (LLIV1). This was accomplished using archival H I emission and absorption data from two 21 cm line surveys:
14 GHIGLS at 9'.4 resolution and DHIGLS at 1' resolution. The spectral decomposition code ROHSA was used to
15 model the column density of different thermal phases and also to analyze an absorption measurement against
16 the radio source 4C +66.09. From the latter we found spin temperature $T_s \sim 75$ K, cold gas mass fraction
17 $f \sim 0.5$, and turbulent sonic Mach number $M_t \sim 3.4$. The cold phase of LLIV1 appears as a collection of
18 elongated filaments that forms a closed structure within the field decomposed. These substructures follow the
19 orientation of the overall large scale cloud, along the diagonal of the GHIGLS field from north-west to south-
20 east (in Galactic coordinates). The angular power spectrum of the cold phase is slightly shallower than that of
21 the warm phase, quantifying that the cold phase has relatively more structure on small scales. Our spatially
22 resolved map of the cold gas mass fraction in LLIV1 reveals significant variations spanning the possible range
23 of f , with mean and standard deviation 0.33 and 0.19, respectively. Similar to the absorption line modeling
24 against 4C +66.09, our best emission line decomposition model has no unstable gas across the whole field of
25 view, suggesting that the thermal condensation and phase transition are not on-going but rather have reached an
26 equilibrium state.

27 **Keywords:** Galaxy: halo – ISM: structure - kinematics and dynamics – Methods: observational - data analysis

1. INTRODUCTION

28 We have surveyed and analyzed the properties of H I
29 line emission in an intermediate latitude field in Ursa Ma-
30 jor ($(\ell, b) = (143^\circ 6, 40^\circ 1)$ or $(\alpha, \delta) = (09^\mathrm{h}41^\mathrm{m}, 68^\circ 33')$),
31 focusing on thermal condensation of warm neutral medium
32 gas (WNM) to cold neutral medium gas (CNM) in the inter-
33 mediate velocity component (IVC). This IVC gas is part of
34 the Low-Latitude Intermediate-Velocity Arch (LLIV) studies
35 by Kuntz & Danly (1996), in particular substructure LLIV1
36 (see their figure 2).

Corresponding author: Luka Vujeva
luka.vujeva@mail.utoronto.ca

38 Maps of LLIV substructures in the velocity range
39 $-60 \text{ km s}^{-1} < v < -30 \text{ km s}^{-1}$, and $-70 \text{ km s}^{-1} < v <$
40 -30 km s^{-1} , respectively, are shown in figures 12(b) and 16,
41 respectively, of Wakker (2001). Their abundances measure-
42 ments using lines of SII, NI, and OI indicate a metallicity
43 that is approximately solar. Absorption of Fe and Si against
44 PG 0804+762 at $(\ell, b) = (138^\circ 3, 31^\circ 0)$ indicates some de-
45 pletion onto dust grains (Richter et al. 2001). There is ther-
46 mal dust emission morphologically correlated with the IVC
47 gas in LLIV (Planck Collaboration XXIV 2011). Wakker
48 (2001) constrain the distance to be in the range 0.9–1.8 kpc
49 ($z = 0.6$ –1.2 kpc). The implied mass is $1.5 - 6 \times 10^5 M_\odot$.
50 Richter et al. (2003) report a relatively high detection rate of
51 H₂ in the IVC gas, implying that CNM is ubiquitous, consis-
52 tent with a key finding of our paper. Absorption lines toward
53 PG 0804+762 (Richter et al. 2001) also indicate a substan-

tial ionization fraction for hydrogen, about 20%. There is also hot coronal gas revealed by O VI absorption toward PG 0804+762 (Richter et al. 2001) and C IV toward SN 1993J (de Boer et al. 1993).

Wakker (2001) notes how this is reminiscent of a Galactic fountain (Shapiro & Field 1976; Bregman 1980; Houck & Bregman 1990), where gas ejected into the Galactic Halo from inside the Solar circle is expected to have a metallicity slightly above that in the local ISM, while the return flow is outside the Solar circle. Planck Collaboration XXIV (2011) show that dust appears to survive the hot phases of the flow (or to reform) and discuss the evolution of dust via shattering. What we find most interesting is that there is a substantial CNM apparently organized with the flow.

Some key elements of the structure of the paper are as follows. In Section 2 we present the H I data used in this work. Evidence for cold gas in LLIV1 based on H I absorption is summarized in Section 3. Section 4 describes the Gaussian decomposition performed to model the H I spectra, Sections 4.2 and 4.3 for GHIGLS and DHIGLS, respectively. Appendices A and C present maps (2D spatial fields) characterizing each Gaussian component (column density, central velocity, velocity dispersion) for the respective data. Identification of the different thermal phases is addressed in Section 4.2.2, with attention to the robustness of the solution (Section 4.2.3). Section 4.2.5 presents a power spectrum analysis of the phase maps (Section 4.2.4). The cold gas mass fraction map inferred from the decomposition of DHIGLS data is analyzed in Section 4.3.4. Finally, a summary is provided in Section 5.

2. H I DATA

2.1. GHIGLS (9°)

We used the GHIGLS¹ 21 cm line survey (Martin et al. 2015) with spatial resolution of 9.4' and velocity resolution and channel spacing of 1.0 km s^{-1} and 0.8 km s^{-1} , respectively, from the Green Bank Telescope (GBT) to examine the brightness temperature T_b of the atomic gas in LLIV1. Specifically, we extracted a 7.5 square sub-region of the NCPL mosaic centered on Galactic coordinates $(144^\circ, +39^\circ)$, the light blue box in Figure 1. The map shows the total integrated column density of the NCPL mosaic in the velocity range $-81 \leq v \leq -27 \text{ km s}^{-1}$ analyzed in this work, covering LLIV1.

Figure 2 shows the mean, median, and standard deviation spectra of data within this sub-region. There is a strong peak near 0 km s^{-1} (hereafter Low Velocity Component (LVC)) that corresponds to gas associated with the NCPL (Taank

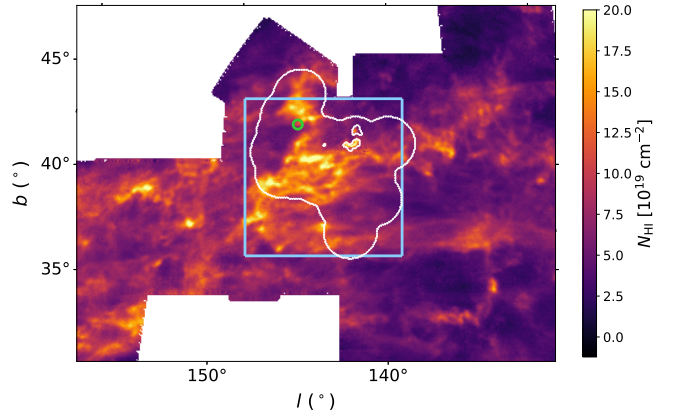


Figure 1. Integrated column density map of the GHIGLS NCPL mosaic in the IVC velocity range $-81 \leq v \leq -27 \text{ km s}^{-1}$ showing the LLIV Arch. The light blue box shows the 128×128 pixel region analyzed. The white contours outlines the DHIGLS UM field and its masks (Section 2.2). The green ring marks the direction of the absorption measurement (Section 3).

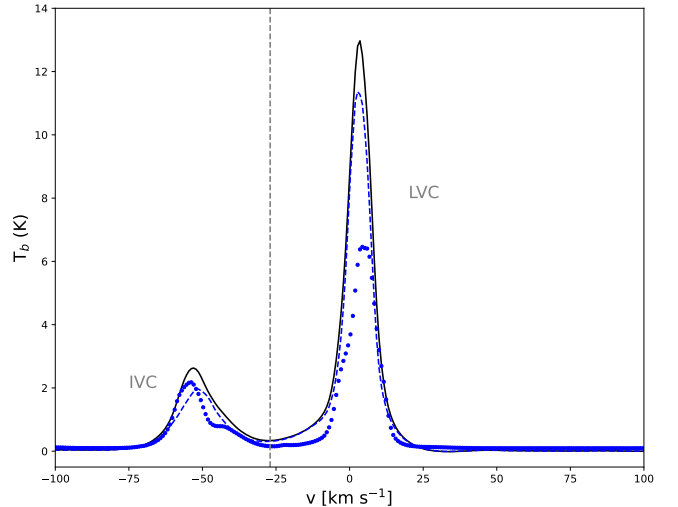


Figure 2. H I spectra characterizing the region analyzed in Ursa Major, the light blue box in Figure 1, showing the LLIV1 and the LVC gas. The black solid, blue dashed and blue dotted lines are the mean, median, and standard deviation spectra, respectively.

et al. 2022). The secondary peak near -55 km s^{-1} is the LLIV1 gas. There is also weak emission in the bridge range between the two components. The ranges were divided at $v = -27 \text{ km s}^{-1}$ (denoted by the vertical line) where the emission in bridge is minimal. Individual channel maps of the mosaic show weak emission in the high velocity range from High Velocity Cloud (HVC) complexes A and C (Planck Collaboration XXIV 2011), extending to velocities close to the IVC range (i.e., $\approx -70 \text{ km s}^{-1}$), but there is very little HVC emission in the region that we analyzed.

¹ GBT H I Intermediate Galactic Latitude Survey: <https://www.cita.utoronto.ca/GHIGLS/>

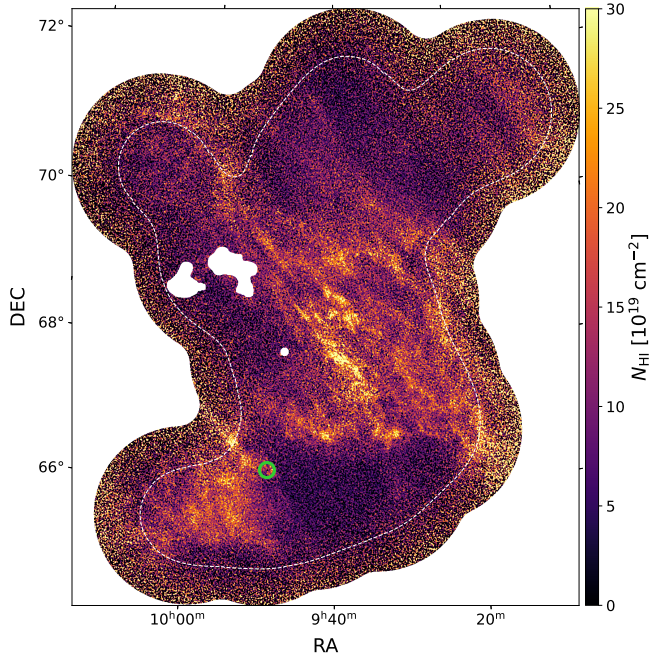


Figure 3. Integrated column density map of the IVC gas in UM from DHIGLS. The white dashed contour indicates where the noise has increased by a factor two relative to the minimum and the three white regions inside show the masks applied to remove extragalactic emission. The green ring marks the direction of the absorption measurement (Section 3).

For the analysis below, pixels contaminated by extra-galactic emission (mainly the M81/82 group) and masked in GHIGLS because of corrupted baselines are in-painted as described in Taank et al. (2022), appendix A.

2.2. DHIGLS ($1'$)

We also made use of the 58 square degree UM dataset that was part of the DHIGLS² H I survey (Blagrade et al. 2017) with the Synthesis Telescope (ST) at the Dominion Radio Astrophysical Observatory. This field is located at $(\alpha, \delta) = (09^{\text{h}}41^{\text{m}}, 68^{\circ}33')$ or $(l, b) = (143^{\circ}6, 40^{\circ}1)$. The 256-channel spectrometer, spacing $\Delta v = 0.824 \text{ km s}^{-1}$ and velocity resolution 1.32 km s^{-1} , was centered at $v_c = -60 \text{ km s}^{-1}$ relative to the Local Standard of Rest (LSR). The spatial resolution of the ST interferometric data was about $1'$. UM is embedded in the NPCL mosaic from GHIGLS shown in Figure 1. The DHIGLS UM T_b data cube has the full range of spatial frequencies, obtained by a rigorous combination of the ST interferometric and GBT single dish data (see section 5 in Blagrade et al. 2017). The pixel size is $18''$.

Figure 3 presents the total column density map of the IVC gas in UM (i.e., LLIV1), whose coverage is also annotated by

the white contour in Figure 1. Note the different native coordinate systems: Equatorial for the DHIGLS data and Galactic for the GHIGLS data. Unlike with the GBT, the higher angular resolution of the ST (i.e., $1'$) allows the detection of high continuum brightness temperature radio point sources, which are useful for H I absorption measurements.

3. EVIDENCE FOR COLD GAS FROM H I ABSORPTION IN LLIV1

Blagrade et al. (2017) reported the detection of CNM gas in the IVC with spin temperature $T_s = 85 \text{ K}$ against the background radio galaxy 4C + 66.09 (NVSS³ J094912 + 661459) with a continuum brightness temperature $T_c = 444 \text{ K}$. This gas is located within LLIV1 as annotated in Figure 1 and related figures.

Following Taank et al. (2022), we used the spectral decomposition code ROHSA (Section 4.1) on the original DHIGLS data to model the emission-absorption pair with Gaussians to refine estimates of the spin temperature and the cold component amplitude and turbulent properties.

We found that the absorption spectrum is well described by a single Gaussian component together with a quadratic polynomial to describe the local residual baseline. Parameters μ_n , σ_n , and T_n of the Gaussian are tabulated in Table 1.

The associated emission line was obtained by averaging data in an annulus centered on the source with an inner radius $r_{\text{in}} = 1.2'$ and an outer radius $r_{\text{out}} = 3'$ (i.e., 4 and 10 pixels of size $18''$, respectively). The resulting spectrum is well fit by the sum of two Gaussians, a narrow and a broad component. Parameters μ_b , σ_b , and T_b of the narrow Gaussian are tabulated in Table 1 (method 1). The CNM mass fraction is $f = 0.51$. Following Blagrade et al. (2017), the numbers from Table 1 lead to a spin temperature of $T_s = 76.3 \text{ K}$, slightly lower than their estimate without profile fitting.

Alternatively, we used ROHSA for a decomposition of emission in a 64×64 pixel grid centered on the source. Again, two Gaussians were needed to fully encode the signal. Parameters μ_b , σ_b , and T_b of the narrower Gaussian at the position of the source were interpolated from the ROHSA parameter maps in the same annulus and are also tabulated in Table 1 (method 2). The CNM mass fraction is $f = 0.55$ and the spin temperature evaluates to $T_s = 72.2$.

Following the procedure described in Taank et al. (2022, see their section 5.1.2), for the CNM line we separated the thermal and non-thermal broadening, σ_{th} and σ_{nt} , respectively, and calculated the associated turbulent Mach number M_t . These are also tabulated in Table 1 for methods 1 and 2.

4. SPECTRAL DECOMPOSITION

² DRAO H I Intermediate Galactic Latitude Survey: <https://www.cita.utoronto.ca/DHIGLS/>

³ NRAO VLA Sky Survey: <https://www.cv.nrao.edu/nvss/>, Condon et al. (1998).

Table 1. Parameters^a of the absorption feature in LLIV1 against 4C +66.09, interpolated emission, and derived T_s , f , and M_t , from DHIGLS data

Method	T_c	μ_n	σ_n	T_n	μ_b	σ_b	T_b	T_s	σ_{th}	σ_{nt}	f	M_t
1	444	2.43	1.52	-109	2.67	1.77	22.41	76.3	0.80	1.31	0.51	3.3
2	444	2.43	1.52	-109	2.66	1.99	22.73	72.2	0.80	1.30	0.55	3.4

^a Velocities in km s^{-1} and temperatures in K.

179

4.1. ROHSA

180 ROHSA is a regularized optimization algorithm that decom-
 181 poses position-position-velocity (PPV) data cubes into a sum
 182 of Gaussians (Marchal et al. 2019). ROHSA takes into account
 183 the spatial coherence of the emission and its multi-phase na-
 184 ture to perform a separation of different thermal phases. The
 185 methodology used in this work is similar to that used in Taank
 186 et al. (2022). We refer the reader to their section 3 for a
 187 comprehensive description of ROHSA and its user-parameters,
 188 including the number of Gaussians N and the set of hyper-
 189 parameters ($\lambda_a, \lambda_\mu, \lambda_\sigma, \lambda_\sigma''$). A ROHSA decomposition requires
 190 the user to choose this set of parameters to obtain a practica-
 191 ble solution and this must be revisited for a given data set
 192 (e.g., Marchal et al. 2021; Taank et al. 2022).

193 Also needed is a noise prescription for the data. For
 194 GHIGLS data, we adopted the 3D prescription discussed by
 195 Boothroyd et al. (2011), $S(v, \mathbf{r}) = S_e(\mathbf{r})(1 + T_b(\mathbf{r})/T_{\text{sys}})$,
 196 where the 2D map of the standard deviation of the noise
 197 $S_e(\mathbf{r})$ is calculated from emission-free end channels (in the
 198 case of GHIGLS, supplied with the archival data), and T_{sys} is
 199 the system temperature, typically 20 K for the GBT L-band
 200 observations. We used the augmented version of the ROHSA
 201 code employed by Taank et al. (2022) to work with 3D noise,
 202 rather than the standard 2D noise. For the DHIGLS data,
 203 we used the original implementation of ROHSA that considers
 204 $S_e(\mathbf{r})$.

4.2. GHIGLS

4.2.1. User parameters

207 The representative solution presented in this work was ob-
 208 tained using the set of parameters $N = 6$, $\lambda_a = \lambda_\mu = \lambda_\sigma = 40$,
 209 and $\lambda_\sigma'' = 50$.

To obtain a solution that fully describes the signal in the IVC range (i.e., LLIV1) without over-fitting the data, we found that $N = 6$ was optimal. This was accomplished by decomposing the data with varying N in the range $N = [5-9]$ and we used the per-channel mean contribution to chi-square,

$$\langle \chi^2(v) \rangle = \sum_r \left(\frac{L(v, \boldsymbol{\theta}(\mathbf{r}))}{S(v, \mathbf{r})} \right)^2 / 128^2, \quad (1)$$

210 to determine the goodness of fit, where $L(v, \boldsymbol{\theta}(\mathbf{r}))$ is the resid-
 211 ual between the Gaussian model and the data. Here the fields

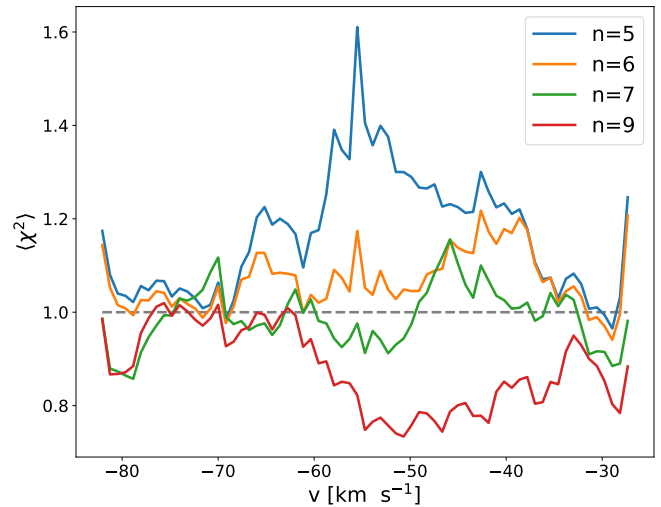


Figure 4. Spectrum of mean contribution to chi-square for Gaussian models fit with different number of Gaussians. Horizontal line indicates $\langle \chi^2 \rangle = 1$.

212 $\boldsymbol{\theta}_n(\mathbf{r}) = (\mathbf{a}_n(\mathbf{r}), \boldsymbol{\mu}_n(\mathbf{r}), \boldsymbol{\sigma}_n(\mathbf{r}))$ – amplitude $\mathbf{a}_n \geq \mathbf{0}$, mean ve-
 213 locity $\boldsymbol{\mu}_n$, and standard deviation $\boldsymbol{\sigma}_n$ – parameterize the N
 214 Gaussians of the model prescribed in ROHSA. Note that 128^2
 215 is the total number of pixels inside the light blue box shown
 216 in Figure 1.

217 Figure 4 shows spectra of the mean contribution to chi-
 218 square $\langle \chi^2(v) \rangle$ for varying N , where $N = 6$ provides a solu-
 219 tion in which $\langle \chi^2(v) \rangle$ is just slightly higher than unity denoted
 220 by the horizontal dashed line. For $N > 6$, $\langle \chi^2(v) \rangle$ is domi-
 221 nated by values lower than unity especially where the signal
 222 is strong, which indicates over-fitting the data.

223 Figure 5 shows a reduced but spatially resolved version of
 224 Equation 1,

$$\chi_r^2(\boldsymbol{\theta}(\mathbf{r})) = \sum_v \left(\frac{L(v, \boldsymbol{\theta}(\mathbf{r}))}{S(v, \mathbf{r})} \right)^2 / k, \quad (2)$$

225 where $k = 69 - 3N$ is the number of degrees of freedom,
 226 with 69 being the number of velocity channels. Spectral data
 227 that were in-painted prior to decomposing the cube were not
 228 considered and are shown as masked regions. Our best model
 229 achieves a mean χ_r^2 across the field of 1.4, with median and
 230 standard deviation of 1.3 and 0.4, respectively.

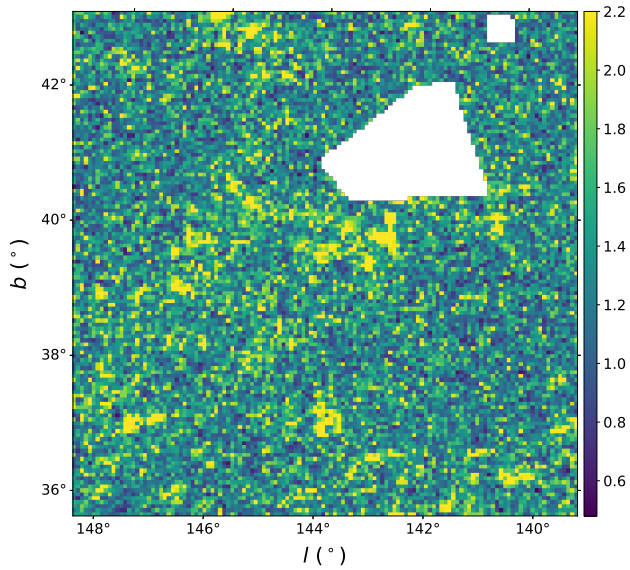


Figure 5. Map of the reduced χ^2_r obtained with ROHSA on the GHIGLS data of LLIV1. Masked regions corresponds to pixels contaminated by extragalactic emission and in-painted before decomposition.

The four hyper-parameters that control the smoothness of the Gaussian parameter maps were chosen to be the same due to the similar functional form of their respective cost functions. This efficiency limits the parameter space explored in finding a practicable solution. They were chosen empirically to correlate adjacent pixels on a spatial scale close to the beam of the instrument. In experimenting with this set of parameters, the optimal model was found to have $\lambda_a = \lambda_\mu = \lambda_\sigma = 40$.

To ensure a solution in which phases are identifiable according to distinct velocity dispersions (phase separation), we explored a range of the λ''_σ parameter, which controls the variance of the normalized velocity dispersion of Gaussian components. We experimented with $\lambda''_\sigma = [1, 10, 20, 50, 100, 500, 1000]$ and found that 50 allows a coherent phase separation (see Section 4.2.2), without adding too much penalty in the global cost function prescribed in ROHSA that would prevent a overall good fit of the data.

4.2.2. A representative solution

The derived Gaussian model parameters for all spatial pixels are summarized in the 2D histogram of the column density-weighted $\sigma - \mu$ parameters in Figure 6. There are six clusters of points that correspond to the N Gaussians used by ROHSA to fit the data. Black points show the column density-weighted average of each cluster, as summarized in Table 2. The distinct average velocity dispersions of the six clusters,

Table 2. Mean kinematic properties (in km s^{-1}) of Gaussians encoding the IVC gas (LLIV1) in the GHIGLS and DHIGLS data

Survey		G_0	G_1	G_2	G_3	G_4	G_5
GHIGLS	$\langle \mu_n \rangle$	-73.6	-58.7	-55.6	-52.9	-48.7	-33.0
	$\langle \sigma_n \rangle$	6.8	5.7	2.1	2.0	5.8	9.08
DHIGLS	$\langle \mu_n \rangle$		-58.2	-55.2	-50.5	-45.7	-26.5
	$\langle \sigma_n \rangle$		6.6	2.3	2.1	5.2	10.0

ranging from about two to nine km s^{-1} , reveal the multiphase nature of the gas in LLIV1.

We observe a clear separation of clusters vertically along the velocity dispersion axis, denoted by the grey horizontal dashed line. G_0 , G_1 , G_4 , and G_5 are broad, typical of warm gas, while G_2 and G_3 are narrow and can be associated with the cold phase of LLIV1. Interestingly, unlike what was found in other fields – LVC from GHIGLS in the North Ecliptic Pole (Marchal et al. 2019; Marchal & Miville-Deschénes 2021) and the NCPL (Taank et al. 2022), and HVC in complex C from DHIGLS in EN (Marchal et al. 2021) – there are no Gaussian components with intermediate dispersion characteristic of lukewarm gas (LNM) associated with a thermally unstable medium. This suggests that in LLIV1 the thermal condensation and phasetransition are not on-going, but rather have reached an equilibrium state.

Horizontally, along the velocity axis, the components G_1 to G_4 are located near the peak of LLIV1 emission as shown in Figure 2. G_0 describes gas in the HVC range that is not of interest in this work and G_5 gas is located in the velocity bridge between emission from the LVC and LLIV1.

The corresponding Gaussian parameter maps, sorted by increasing mean velocity, are presented in Appendix A. Column density, velocity, and dispersion velocity maps of the six Gaussian components are shown in Figures A1, A2, and A3, respectively. By visualizing each column density map, we found that G_1 , G_2 , G_3 , and G_4 show a morphological correlation not shared with G_0 and G_5 . In the following sections, only the four Gaussian components between the two vertical dashed lines in Figure 6 were kept.

4.2.3. Uncertainties

To explore the degeneracy of the solution, we generated a model cube from the representative solution shown in Figure 6, and we repeated the Gaussian decomposition using three series of runs (Marchal et al. 2021; Taank et al. 2022). The first series explores how the outcome of the decomposition is influenced by the injection of 50 different instance of the noise. The hyper-parameters were kept the same. The second series explores the impact of the hyper-parameters on the solution. It entails generating 50 runs using random

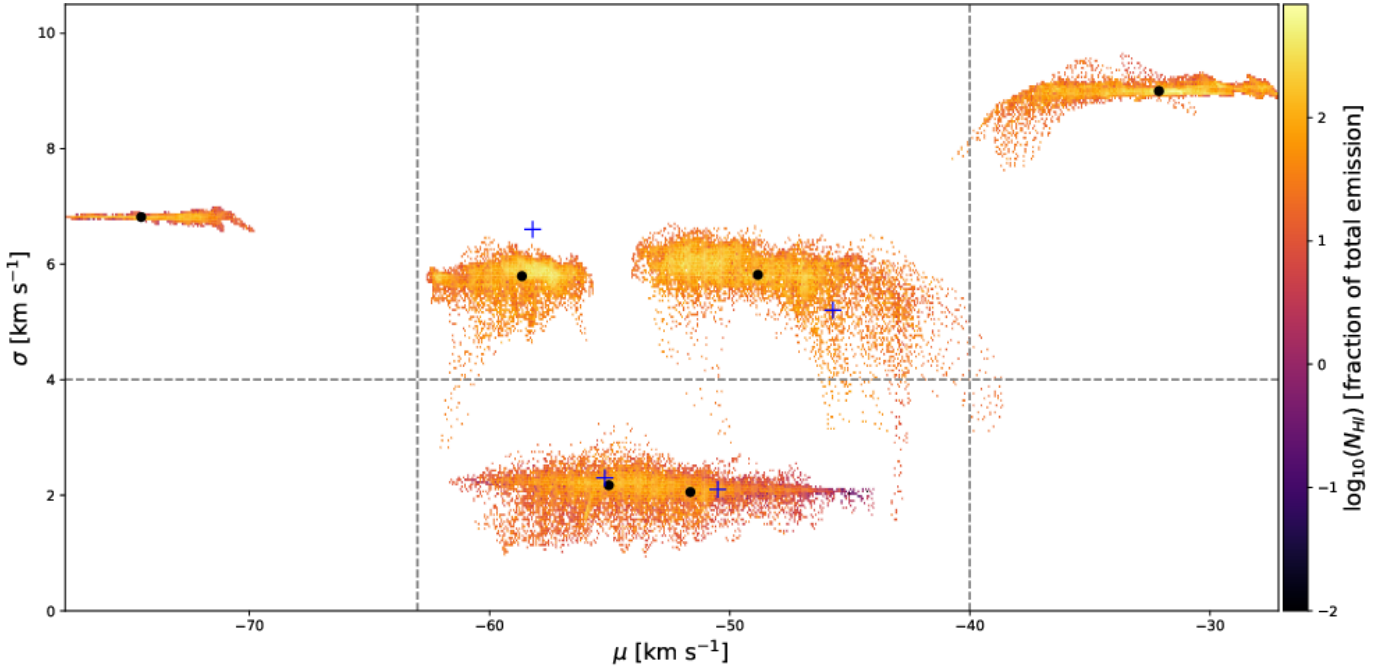


Figure 6. Two-dimensional probability distribution function of σ and μ of the six Gaussians, weighted by their column densities obtained by decomposing the GHIGLS data of LLIV1 with ROHSA. The black dots correspond to the column density means of each cluster. The blue crosses show the same quantity but for the decomposition of the DHIGLS data within the selected velocity range. The horizontal dotted grey line shows the separation between the identified two thermal phases. The vertical grey lines show the velocity range where Gaussian components encodes emission from LLIV1.

297 perturbations of the four ROHSA hyper-parameters in a $\pm 10\%$
 298 interval around the original values. Here, the injected 3D
 299 Gaussian random was kept the same. The third explores the
 300 sensitivity to how ROHSA is initialized by generating 50 runs
 301 where the four Gaussians needed to initialize ROHSA are ran-
 302 domly selected from the original $\sigma - \mu$ diagram shown in
 303 Figure 6. We refer the reader to Taank et al. (2022) for fur-
 304 ther details of the procedure.

305 For each of the 50-run series, the outcomes were examined
 306 in $\sigma - \mu$ space, showing that the clusters observed in Figure 6
 307 are quite stable, including the lack of components with inter-
 308 mediate velocity dispersions. For each run, we performed a
 309 phase separation by grouping the four Gaussians into two cat-
 310 egories based on their mean velocity dispersion; Gaussians
 311 with $\langle \sigma_n \rangle > 4 \text{ km s}^{-1}$ were classified as WNM and Gaus-
 312 sians with $\langle \sigma_n \rangle < 4 \text{ km s}^{-1}$ were classified as CNM. For
 313 each series, maps of the mean column density and its stan-
 314 dard deviation were generated for the two components. All
 315 50 runs of each series were combined to calculate maps of
 316 column density and corresponding standard deviations. Fi-
 317 nally, the contributions from the three series were summed in
 318 quadrature to yield the total uncertainty.

4.2.4. Phase maps

319 Figure 7 shows the column density maps (first column)
 320 with their associated uncertainty maps (second column) of
 321 the cold (top) and warm phases (bottom) in the GHIGLS
 322

323 data of LLIV1. Although we note some variations of the
 324 uncertainties across the field, their low values relative to the
 325 associated column densities reflects the high stability of the
 326 solution found with ROHSA.

327 The cold phase of LLIV1 appears as a collection of elon-
 328 gated filaments that forms a closed structure within the de-
 329 composed field. These substructures seem to follow the ori-
 330 entation of the overall large scale cloud, along the diagonal
 331 of the field from north-west to south-east (Galactic coordi-
 332 nates). The column density of the more diffuse warm phase
 333 is highest within the contour delimited by the presence of
 334 cold gas, but also exists outside of LLIV1. There is a corre-
 335 lation of cold gas mass fraction f with the total gas column
 336 density, as seen in Figure 8.

337 The CNM substructures reassemble structures seen in the
 338 total column density map shown in Figure 1, which indicates
 339 that the cold gas mass in LLIV1 is relatively high. Beyond
 340 what is seen statistically in Figure 8, this will be quantified
 341 spatially in Section 4.3.4.

4.2.5. Power spectrum

342 We statistically quantified and compared the multi-scale
 343 structure of the two phases by calculating their power spec-
 344 trum $P(k)$, the azimuthal average of the modulus of the
 345 Fourier transform of their column density field. We modelled
 346 them as $P(k) = B(k) \times P_0 k^\gamma + A \times N(k)$, where P_0 is the ampli-
 347 tude of the power spectrum, γ is the scaling exponent, $B(k)$

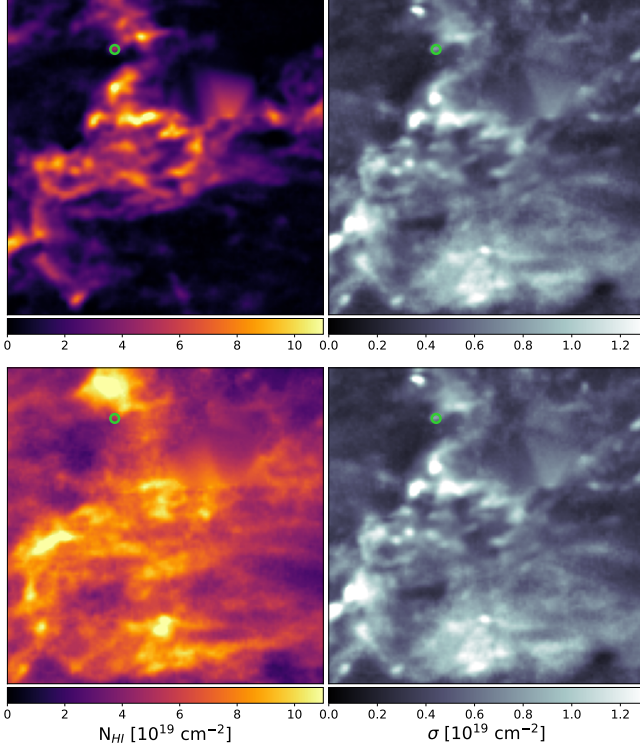


Figure 7. Column density maps (first column) with their associated uncertainties (second column) of the cold (top) and warm (bottom) phases in the GHIGLS data of LLIV1. The green ring marks the position of the absorption feature against 4C +66.09.

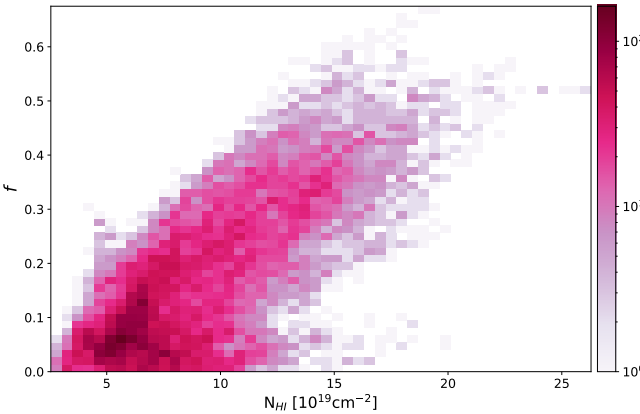


Figure 8. 2D histogram of the CNM mass fraction from the GHIGLS solution with respect to the total \$N_{HI}\$.

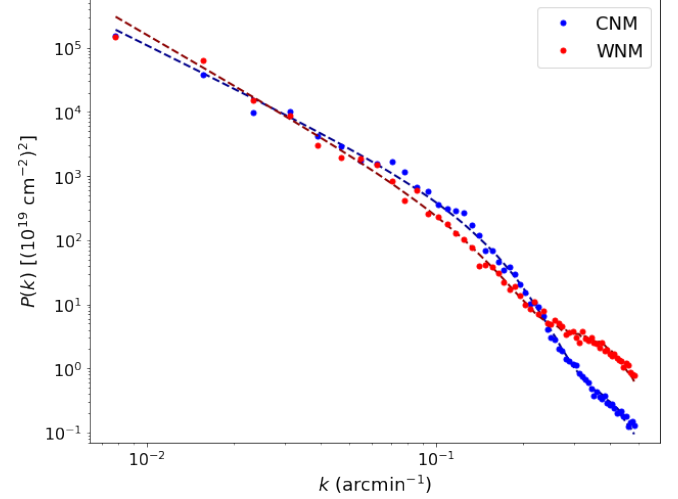


Figure 9. Angular power spectra \$P(k)\$ of the integrated column density of the cold (blue) and warm (red) phases. The dashed lines represent the models fit to each phase independently.

Figure 9 show \$P(k)\$ for the cold and warm phases, in blue and red dots respectively. The total fitted model is shown by the dashed dark blue and red lines for the cold and warm phases respectively. Recognizing the uncertainties, we find that the scaling exponent for the cold phase \$\gamma_{\text{CNM}} = -2.230 \pm 0.002\$ is higher than that of the warm phase with \$\gamma_{\text{WNM}} = -2.613 \pm 0.003\$. In other words, the power spectrum of the cold phase is slightly shallower than that of the warm phase, quantifying that the cold phases have relatively more structure on small scales. This is similar to what was found by Marchal & Miville-Deschénes (2021) and Marchal et al. (2021) in high latitude solar neighborhood gas of the NEP field of the GHIGLS survey, and the HVC complex C analyzed with DHIGLS data (the EN field).

4.3. DHIGLS

4.3.1. Initialization

We performed a first exploration of the user-parameters using the same methodology as described in Section 4.2.1. This search resulted in a set of parameters (\$N = 5, \lambda_a = \lambda_\mu = \lambda_\sigma = 10, \lambda_\sigma'' = 10\$) that could satisfy our selection criteria, including the flat \$\chi_r^2\$ map with a mean value close to unity. This solution although statistically good was found to be impracticable. After generated the model cube and applying a convolution to both the model and the data to lower their spatial resolution, the model was no longer providing a good description of the data. Specifically, the solution was found to have only one narrow Gaussian to describe the cold gas while the convolved data show two distinct peaks at a resolution as low as 2'. Figure B4 illustrates this by showing the original data (black line), and the convolved data at 2' and

describes the cutoff of the spectrum at high \$k\$ due to the beam of the instrument, assumed to be a 2D Gaussian of FWHM = 9'.4, and \$N(k)\$ is the noise estimated by taking the power spectrum of empty channel maps of the PPV cube and scaled by a multiplicative factor \$A\$. The finite images were apodized using a cosine function to minimize systematic edge effects from the implementation of the Fourier transform.

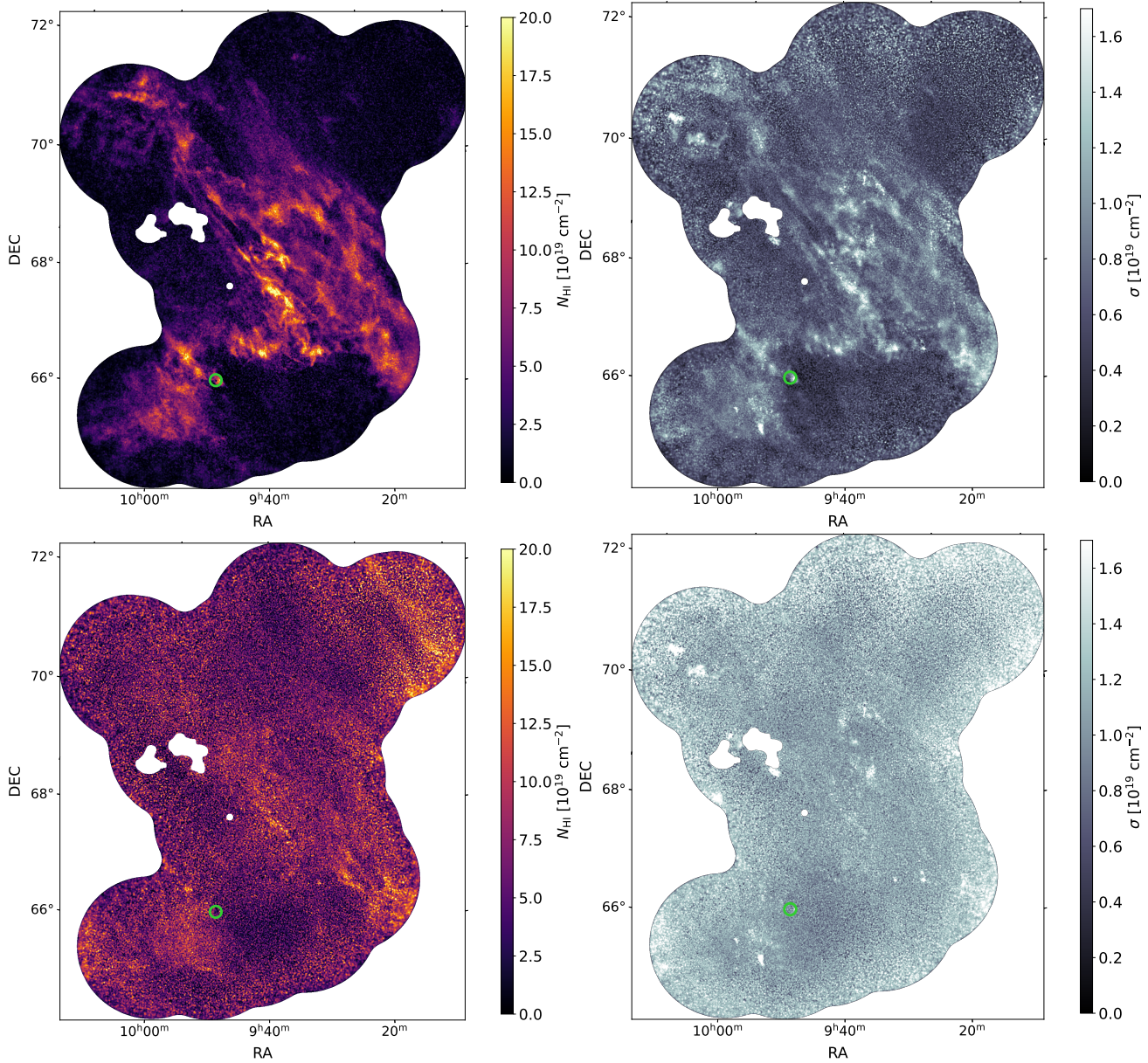


Figure 10. Column density maps (first column) with their associated standard deviation maps (second column) of the cold (top) and warm (bottom) phases from the DHIGLS data in LLIV1. The green ring marks the position of the absorption measurement against 4C +66.09.

9'.4 with a green line and blue line, respectively. The model fit to the DHIGLS data is shown by the red line.

To obtain a consistent solution at various resolution (from the native 1' beam to the 9'.4 beam of the GHIGLS data), we used the value tabulated in Table 2 as initial parameters to start the multi-resolution prescribed in ROHSA (Marchal et al. 2019; Taank et al. 2022). Only the five components whose mean velocities were included in the velocity range covered by the DHIGLS data where used; Gaussians G_1 to G_5 .

395

4.3.2. Solution and Uncertainties

An appropriate set of hyper-parameters was found to be $(\lambda_a = \lambda_\mu = \lambda_\sigma = 10, \lambda''_\sigma = 10)$. The resulting decomposition still satisfies all our selection criteria, with a fairly uniform χ^2_r map (not shown here), showing no evidence of an overfitting of the data.

The mean kinematic properties of the five Gaussians used to describe the DHIGLS data are tabulated in Table 2; labeled from G_1 to G_6 . Values of the components G_1 to G_4 (associated to LLIV1) are also denoted by blue crosses in Figure 6, and appear to be fairly consistent with those obtained from the decomposition of the GHIGLS data.

The corresponding Gaussian parameter maps, sorted by increasing mean velocity, are presented in Appendix C. Column density maps, velocity maps, and dispersion velocity maps of the five Gaussian components are shown in Figure C5. Visualization of each column density map shows similar morphology (and morphological correlation between components) than that of the GHIGLS solution, described in Section 4.2.2. Building on this solution, we followed the same methodology as described in Section 4.2.3 to evaluate the mean column density and uncertainty maps for each phase. The top and bottom panels in Figure 10 show the resulting maps for the cold and warm phases, respectively.

4.3.3. Comparison with GHIGLS

Our modeling of the cold phase in LLIV1 at high resolution ($1'$) reveals similar large scale properties as the $9.4'$ modeling obtained with GHIGLS data; the cold phase seems to be confined within a closed contour, surrounded by or mixed in with its warm counterpart. The global orientation of LLIV1 and the filamentary structures within suggests that there is a bulk motion of the gas cloud on the plane of the sky (from top left to bottom right in Equatorial coordinates).

The cold filamentary structures appear thinner at this resolution and the width of some filaments likely reaches the size of the $1'$ beam of the ST. This is notably the case for the highly elongated filament seen at the edge of the cloud located on the right hand side of the masked regions within the field, and oriented along its diagonal (from top left to bottom right). Clustering those filaments and analyzing their statistical properties is beyond the scope of this paper but will provide in the further work valuable insight about the thermal condensation that has occurred in LLIV1.

4.3.4. CNM mass fraction

The left panel in Figure 11 shows our best model of the cold gas mass fraction $f(\mathbf{r})$ in LLIV1 at the $1'$ resolution of the ST, and the left panel shows the corresponding uncertainties. $f(\mathbf{r})$ shows large variations across the field and even within the contour delimiting the large scale extent of the cold phase. The mean and standard deviation of $f(\mathbf{r})$ are 0.33 and 0.19, respectively. Interpolated at the position of the absorption measurement against $4C +66.09$, $f(\mathbf{r})$ is 0.46 ± 0.06 , close to the values tabulated in Table 1.

The spatial distribution (i.e., morphological structure) of $f(\mathbf{r})$ reassemble the column density map of the cold phase only, due to a relatively constant (i.e., flat) column density observed in the warm phase within the sky coverage of the DHIGLS data. Specifically, $f(\mathbf{r})$ shows the same elongated filaments, as well as finger-like structures which seem to be part of an organized series of scalloping structures at the edge of LLIV1 oriented perpendicularly to the main orientation of the cloud and large filaments. This is particularly reminiscent of the structure observed in the Draco Nebula (Miville-

Deschênes et al. 2017, and references therein), another IVC that is thought to be part of the Galactic fountain process.

5. SUMMARY

Our novel study of the multi-phase properties of LLIV1 is based on H I spectra from GHIGLS and DHIGLS. We used ROHSA to decompose the spectral data in emission to model their multiphase structure and corroborated this with analysis of an absorption spectrum. The main conclusions are as follows.

- From the absorption line measurement in LLIV1 against $4C +66.09$, we find spin temperature $T_s \sim 75$ K, cold gas mass fraction $f \sim 0.5$ (with no component associated with a thermally unstable medium), and turbulent sonic Mach number $M_t \sim 3.4$, characteristic of supersonic turbulence in the cold phase.
- The cold phase of LLIV1 appears as a collection of elongated filaments that forms a closed structure within the field decomposed. These substructures follow the orientation of the overall large scale cloud, along the diagonal of the GHIGLS field from northwest to south-east (in Galactic coordinates).
- The column density of the more diffuse warm phase is highest within the contour delimiting the presence of cold gas, but also exists outside of LLIV1.
- The angular power spectrum of the cold phase is slightly shallower than that of the warm phase, quantifying that the cold phase has relatively more structure on small scales.
- Our spatially resolved map of the cold gas mass fraction in LLIV1 is consistent with the absorption measurement against $4C +66.09$ and reveals significant variations spanning the possible range of f , with mean and standard deviation of 0.33 and 0.19, respectively.
- Similar to the absorption line modeling against $4C +66.09$, our best emission line decomposition model has no unstable gas across the whole field of view, suggesting that the thermal condensation and phase transition are not on-going but rather have reached an equilibrium state.

ACKNOWLEDGMENTS

We acknowledge support from the Natural Sciences and Engineering Research Council (NSERC) of Canada. Some of this work was carried out when LV and MT participated in the Summer Undergraduate Research Program (SURP) hosted by the University of Toronto. This research made use of the NASA Astrophysics Data System.

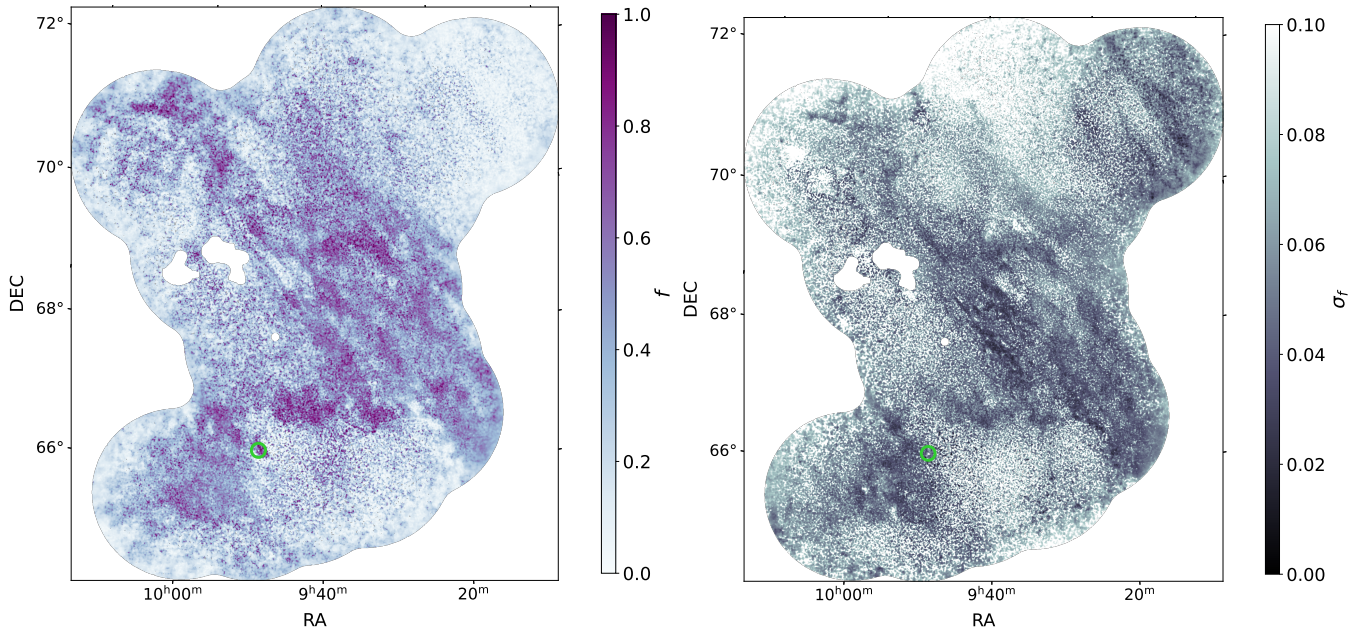


Figure 11. CNM mass fraction map inferred from the DHIGLS data.

⁴⁹⁷ *Software:* Matplotlib (Hunter 2007), NumPy (van der
⁴⁹⁸ Walt et al. 2011), and AstroPy⁴, a community-developed
⁴⁹⁹ core Python package for Astronomy (Astropy Collaboration

⁵⁰⁰ et al. 2013, 2018), SciPy (Virtanen et al. 2020), scikit-image
⁵⁰¹ (van der Walt et al. 2014).

502

APPENDIX

503 **A. PARAMETER MAPS OF INDIVIDUAL GAUSSIAN
 504 COMPONENTS (GHIGLS)**

505 Figure A1 shows the column density maps of each Gaus-
 506 sian sorted by increasing column density-weighted mean ve-
 507 locities (see Table 2). Figures A2 and A3 shows the corre-
 508 sponding velocity fields and dispersion velocity fields. Note,
 509 the labels overlaid on the panels in Figure A1 help to asso-
 510 ciate them with the clusters in Figure 6: e.g., for G_2 (row 2,
 511 column 1), “ G_2 CNM 2.1” indicates the name of the Gaus-
 512 sian component, the thermal phase, and the column density-
 513 weighted mean velocity dispersion $\langle \sigma_n \rangle$ in km s^{-1} as tabu-
 514 lated in Table 2.

515 **B. IMPACT OF SPATIAL RESOLUTION ON THE LINE**

516 Figure B4 illustrates the impact of spatial resolution on a
 517 line of sight within the DHIGLS field of view chosen for its
 518 distinct double peaks property. The purple line shows the
 519 original DHIGLS data, and the red and blue line show the
 520 same data but convolved at 2' and 9.4', respectively.

521 **C. PARAMETER MAPS OF INDIVIDUAL GAUSSIAN
 522 COMPONENTS (DHIGLS)**

⁴ <http://www.astropy.org>

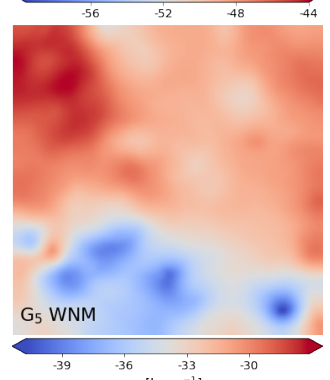
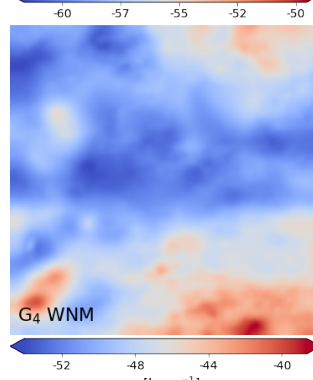
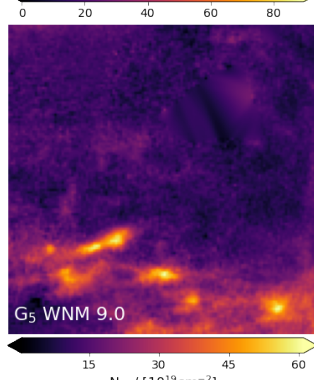
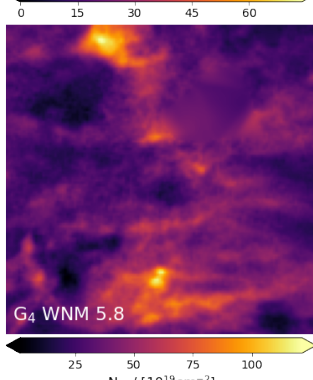
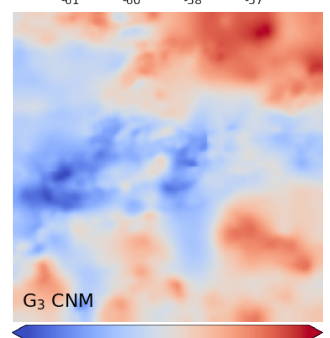
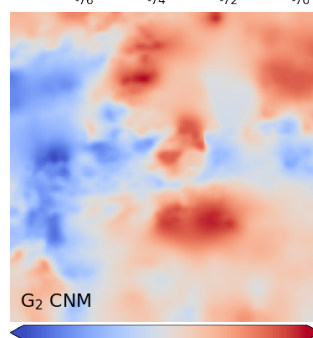
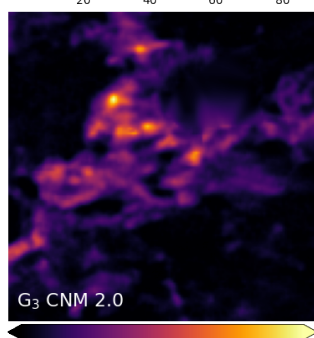
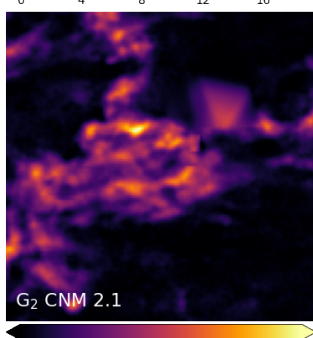
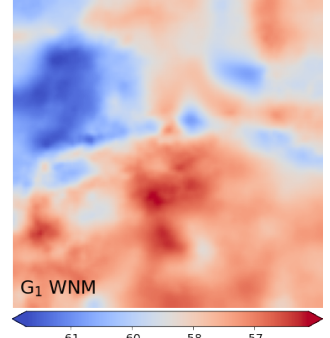
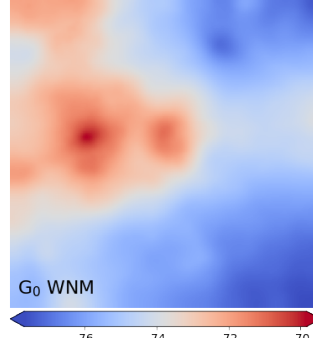
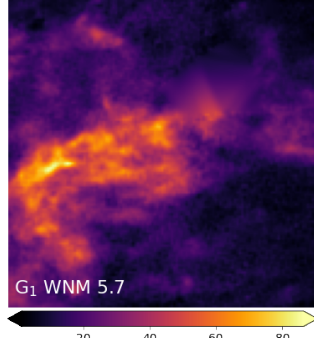
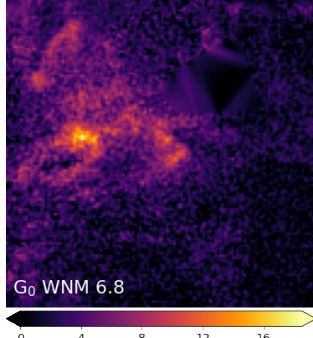


Figure A1. Mosaic of N_{HI} maps of the individual Gaussian components. The maps are sorted by mean velocity. The labels in the bottom left corner represent the sorting of that particular Gaussian component. The number is the mean velocity dispersion (σ) in units of km s^{-1} .

Figure A2. Mosaic like Fig. A1, but of maps of the mean velocity μ of the Gaussian components.

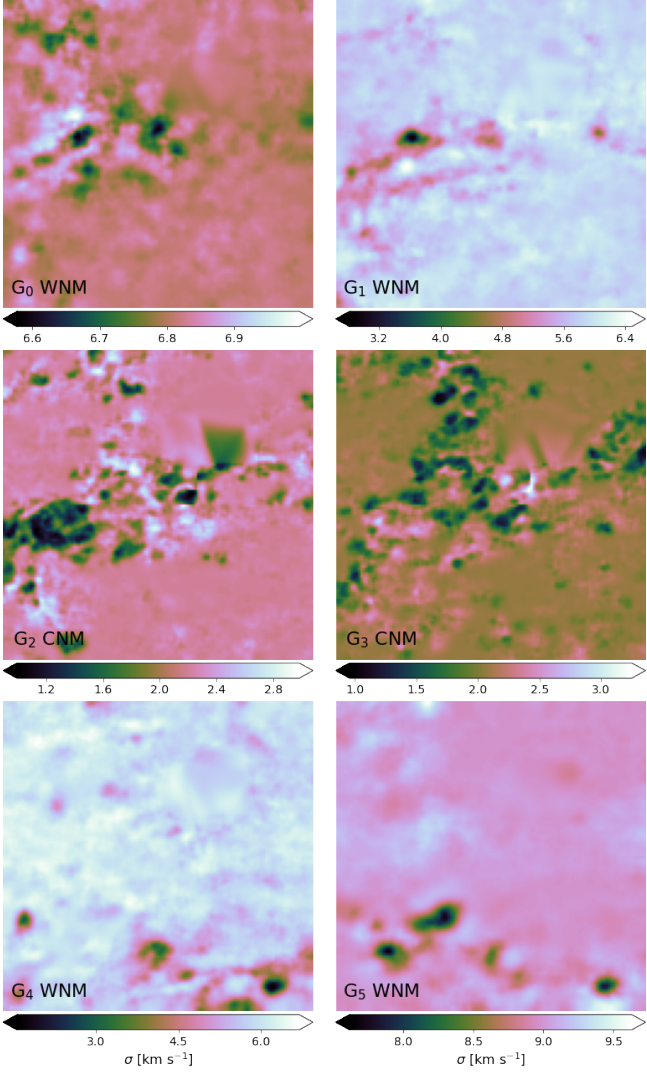


Figure A3. Mosaic like Fig. A1, but of maps of the velocity dispersion σ of the Gaussian components.

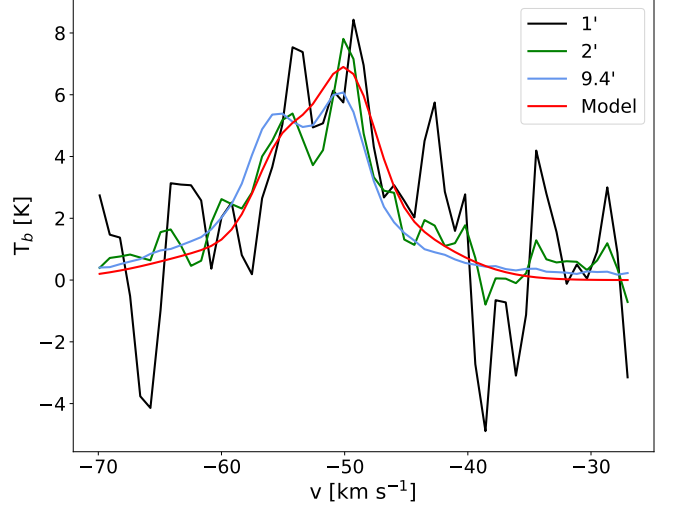


Figure B4. Spectrum showing a double peak of cold gas within the DHIGLS field of view. The black line shows the original DHIGLS data, and the green and blue line show the same data but convolved at 2' and 9.4', respectively. The red line shows the model fit to the DHIGLS data at 1'.

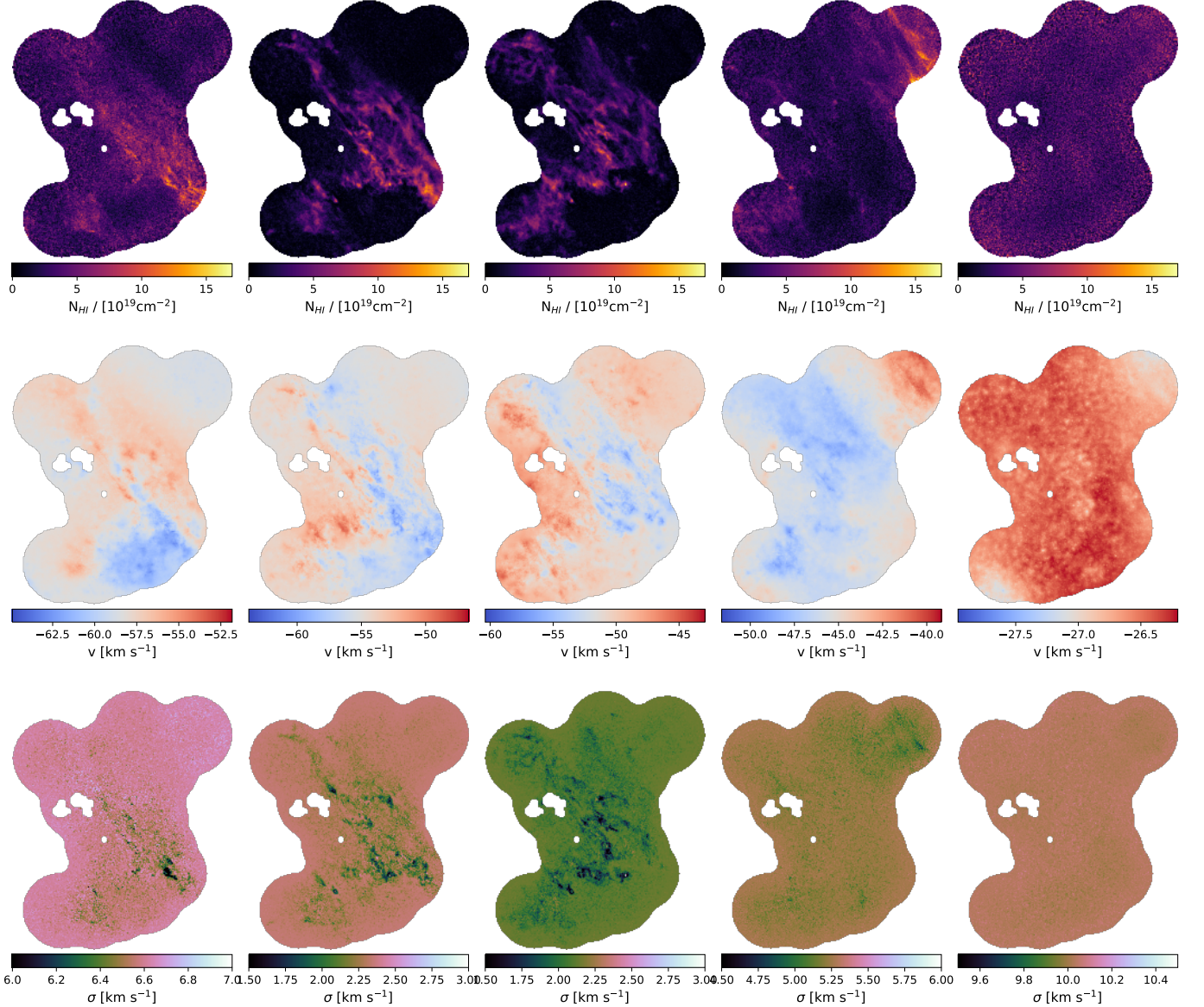


Figure C5. Column density maps (top) of Gaussian components identified in the IVC gas (incl. LLIV1) from the DHIGLS data. The middle and bottom rows show the corresponding velocity maps and dispersion velocity maps, respectively.

REFERENCES

- 523 Astropy Collaboration, Robitaille, T. P., Tollerud, E. J., et al. 2013,
 524 A&A, 558, A33, doi: [10.1051/0004-6361/201322068](https://doi.org/10.1051/0004-6361/201322068)
- 525 Astropy Collaboration, Price-Whelan, A. M., Sipőcz, B. M., et al.
 526 2018, AJ, 156, 123, doi: [10.3847/1538-3881/aabc4f](https://doi.org/10.3847/1538-3881/aabc4f)
- 527 Blagrave, K., Martin, P. G., Joncas, G., et al. 2017, ApJ, 834, 126,
 528 doi: [10.3847/1538-4357/834/2/126](https://doi.org/10.3847/1538-4357/834/2/126)
- 529 Boothroyd, A. I., Blagrave, K., Lockman, F. J., et al. 2011, A&A,
 530 536, A81, doi: [10.1051/0004-6361/201117656](https://doi.org/10.1051/0004-6361/201117656)
- 531 Bregman, J. N. 1980, ApJ, 236, 577, doi: [10.1086/157776](https://doi.org/10.1086/157776)
- 532 Condon, J. J., Cotton, W. D., Greisen, E. W., et al. 1998, AJ, 115,
 533 1693, doi: [10.1086/300337](https://doi.org/10.1086/300337)
- 534 de Boer, K. S., Rodriguez Pascual, P., Wamsteker, W., et al. 1993,
 535 A&A, 280, L15
- 536 Houck, J. C., & Bregman, J. N. 1990, ApJ, 352, 506,
 537 doi: [10.1086/168554](https://doi.org/10.1086/168554)
- 538 Hunter, J. D. 2007, CSE, 9, 90, doi: [10.1109/MCSE.2007.55](https://doi.org/10.1109/MCSE.2007.55)
- 539 Kuntz, K. D., & Danly, L. 1996, ApJ, 457, 703,
 540 doi: [10.1086/176765](https://doi.org/10.1086/176765)
- 541 Marchal, A., Martin, P. G., & Gong, M. 2021, ApJ, 921, 11,
 542 doi: [10.3847/1538-4357/ac0e9d](https://doi.org/10.3847/1538-4357/ac0e9d)
- 543 Marchal, A., & Miville-Deschénes, M.-A. 2021, ApJ, 908, 186,
 544 doi: [10.3847/1538-4357/abd108](https://doi.org/10.3847/1538-4357/abd108)
- 545 Marchal, A., Miville-Deschénes, M.-A., Orieux, F., et al. 2019,
 546 A&A, 626, A101, doi: [10.1051/0004-6361/201935335](https://doi.org/10.1051/0004-6361/201935335)
- 547 Martin, P. G., Blagrave, K. P. M., Lockman, F. J., et al. 2015, ApJ,
 548 809, 153, doi: [10.1088/0004-637X/809/2/153](https://doi.org/10.1088/0004-637X/809/2/153)
- 549 Miville-Deschénes, M. A., Salomé, Q., Martin, P. G., et al. 2017,
 550 A&A, 599, A109, doi: [10.1051/0004-6361/201628289](https://doi.org/10.1051/0004-6361/201628289)
- 551 Planck Collaboration XXIV. 2011, A&A, 536, A24,
 552 doi: [10.1051/0004-6361/201116485](https://doi.org/10.1051/0004-6361/201116485)
- 553 Richter, P., Savage, B. D., Wakker, B. P., Sembach, K. R., &
 554 Kalberla, P. M. W. 2001, ApJ, 549, 281, doi: [10.1086/319070](https://doi.org/10.1086/319070)
- 555 Richter, P., Wakker, B. P., Savage, B. D., & Sembach, K. R. 2003,
 556 ApJ, 586, 230, doi: [10.1086/346204](https://doi.org/10.1086/346204)
- 557 Shapiro, P. R., & Field, G. B. 1976, ApJ, 205, 762,
 558 doi: [10.1086/154332](https://doi.org/10.1086/154332)
- 559 Taank, M., Marchal, A., Martin, P. G., & Vujeva, L. 2022, ApJ,
 560 937, 81, doi: [10.3847/1538-4357/ac8b86](https://doi.org/10.3847/1538-4357/ac8b86)
- 561 van der Walt, S., Colbert, S. C., & Varoquaux, G. 2011, CSE, 13,
 562 22
- 563 van der Walt, S., Schönberger, J. L., Nunez-Iglesias, J., et al. 2014,
 564 PeerJ, 2, e453, doi: [10.7717/peerj.453](https://doi.org/10.7717/peerj.453)
- 565 Virtanen, P., Gommers, R., Oliphant, T. E., et al. 2020, Nature
 566 Methods, 17, 261,
 567 doi: <https://doi.org/10.1038/s41592-019-0686-2>
- 568 Wakker, B. P. 2001, ApJS, 136, 463, doi: [10.1086/321783](https://doi.org/10.1086/321783)